PAPER

Check for updates

Biaxial pseudorotaxane secondary assembly for phosphorescent cellular imaging†

Yao-Hua Liu, Mian Tang, Xiaolu Zhou and Yu Liu [ID] *

Herein, we report a biaxial pseudorotaxane supramolecular optical probe, which was constructed from cucurbit[8]uril (CB[8]) encapsulating a double cationic bromophenol pyridinium salt derivative (BPTN) and co-assembled with disulfide-pillar[4]arene (SSP[4]). Compared with BPTN, the biaxial pseudo-rotaxane obtained with a binding ratio of 1:2 between CB[8] and BPTN not only effectively induced the phosphorescence of BPTN through macrocyclic confinement, but also further assembled with SSP[4] leading to the quenching of phosphorescence. Interestingly, the non-phosphorescent supramolecular assembly can respond to pH 6.5 or excess glutathione (GSH) to disassemble, resulting in recovery of phosphorescence. Cell experiments showed that this process can be specifically achieved in the microenvironment of cancer cells rather than normal cells, performing as a dual-responsive phosphorescent supramolecular probe for the targeted imaging of cancer cells. Therefore, this work provides a convenient supramolecular strategy for the construction of phosphorescent probe targeting cancer cells.

Introduction

Supramolecular stimuli-response systems have been widely studied for drug delivery, bio-imaging, and theranostics based on dynamic and reversible noncovalent interactions.[1,2] Among various stimulations, those systems responsive to internal endogenous stimuli, including pH, glucose, glutathione, adenosine triphosphate (ATP), hypoxia and enzymes, provide an efficient way to mimic the processes of natural biological systems.[3] Considering different pathological profiles in normal cells/tissues and tumour microenvironment, those systems can obtain enhanced imaging or treatment results in the targeted cells or tissues compared to the surrounding environment.[4,5] Such a strategy makes smaller lesions and abnormalities easier to detect compared with traditional methods.[6] Therefore, the endogenous stimuli-response supramolecular assembly systems can detect pathological properties in the diseased area and provide disease progression.[7–10]

On the other hand, purely organic room temperature phosphorescent (RTP) materials have attracted the attention of many researchers and have achieved a series of results in bioimaging, sensing, organic light-emitting diodes and data encryption.[11–15] However, most RTP materials are solid-state and water-insoluble, while amorphous RTP systems in aqueous

solution are seriously affected by quenching by oxygen and water.[16] Despite these headwinds, researchers have still put in the effort and have successfully developed a variety of RTP systems in aqueous solution.[17–20] A series of strategies, such as aggregation,[15,21] a rigid matrix[22] and supramolecular host–guest interactions,[17,23,24] have been proposed. In particular, amorphous host–guest RTP systems using supramolecular macrocyclic compounds (*e.g.*, cucurbiturils (CBs) or cyclodextrins (CDs)) have attracted wide attention owing to their simple preparation, diverse molecular structures and tunable performance.[25] For example, George and co-workers have reported a supramolecular assembly with efficient RTP in aqueous solution using host–guest encapsulation with CB[7] or an electrostatic supramolecular scaffolding using LAPONITE® clays.[19] In addition, we have designed a supramolecular nanosystem composed of CB[8] and an anthracene derivative, which can achieve fluorescence–phosphorescence conversion and a dual organelle imaging response to UV irradiation.[26] In particular, RTP systems show a greater advantage in achieving high signal-to-noise ratio in bioimaging compared to traditional fluorescence imaging systems.[27] Benefiting from their long lifetime and large Stokes shift, RTP systems may obtain clearer and more accurate images by filtering out background fluorescence from biological tissue or cells.[21,28] Regardless of these remarkable studies, the development of efficient endogenous stimuli approaches to regulate phosphorescent behavior still remains an urgent challenge at the supramolecular level.

In line with this idea, we have constructed a supramolecular assembly with RTP emission responding to reduced

glutathione (GSH) or a weakly acidic environment. In this work, a bromophenyl pyridinium derivative (BPTN) with double cations can form a supramolecular pseudorotaxane with CB[8] *via* host–guest interaction emitting green RTP in aqueous solution. The addition of an S–S bond bridged pillar[4]arene[29,30] (SSP[4]) made the pseudorotaxane further assemble into supramolecular nanoparticles through electrostatic interaction and at the same time led to the quenching of phosphorescence. Moreover, weak acidity leading to partial protonation of SSP[4] or the addition of GSH resulting in the destruction of the macrocyclic structure of SSP[4] can both cause the supramolecular nanoparticles to disassemble. Thus, the RTP of the pseudorotaxane was restored. More interestingly, such endogenous stimuli responsive RTP can be achieved in cancer cells rather than normal cells. Therefore, it is believed that such supramolecular strategies provide a convenient method for phosphorescence imaging and disease diagnosis.

Results and discussion

The synthesized bromophenyl pyridinium derivative (BPTN) with double cations is shown in the Scheme 1, whose synthesis and characterization are detailed in the supporting information (Fig. S1–S4, ESI†). Firstly, nuclear magnetic resonance (NMR) spectroscopy was carried out to explore the nature of the host–guest interaction between two kinds of CBs (CB[7] and CB[8]) and BPTN. With the addition of CB[7], protons H_a, H_b, H_c and H_d on the bromophenyl pyridinium shifted to high field with passivation showing the bromophenyl pyridinium group was in the cavity of CB[7] (Fig. S5, ESI†). There was no change in the chemical shift of H_i, H_j or H_e. The proton signals of the methylene group (H_h) adjacent to the pyridyl group were covered by HDO, so it cannot be accurately analyzed. Nevertheless, we can still judge that CB[7] enveloped the bromophenyl pyridinium group of BPTN. As for CB[8], new signals were present in the low-field region of BPTN, and the old signals were reduced to disappearance, showing a representative slow exchange phenomenon where both free BPTN and a
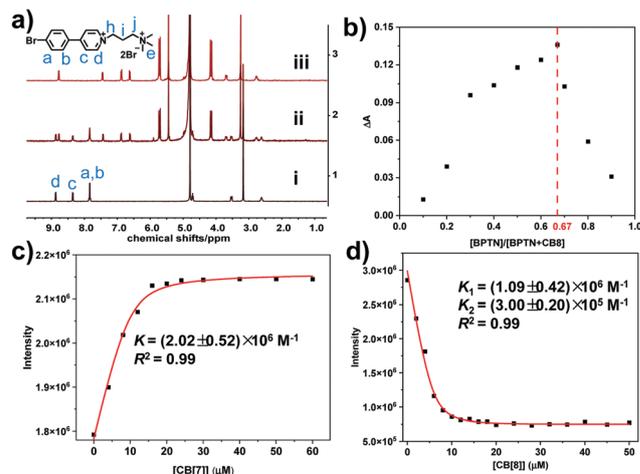

Fig. 1 (a) ^{1}H NMR spectroscopy of BPTN with (i) 0, (ii) 0.25 and (iii) 0.5 eq. CB[8] in D$_2$O at 298 K; (b) Job's plot of BPTN and CB[8] in PBS solution ([BPTN] + [CB[8]] = 50 μM) at 298 K; (c) nonlinear least-squares fit of the change in absorbtion of the BPTN (10 μM) peaks as a function of CB[7] concentration (0–60 μM) in PBS solution at 298 K; (d) nonlinear least-squares fit of the change in absorbtion of the BPTN (10 μM) peaks as a function of CB[8] concentration (0–50 μM) in PBS solution at 298 K.

BPTN⊂CB[8] complex exist in solution (Fig. 1a). In detail, upfield shifts of 1.22, 0.96, 0.93 and 0.10 ppm for the bromophenyl pyridinium protons H_a, H_b, H_c and H_d, respectively, were observed in the ^{1}H NMR spectrum, indicating that the bromophenyl pyridinium group was in the cavity of CB[8]. Simultaneously, downfield shifts of 0.17, 0.15 and 0.08 ppm for the protons H_j, H_i and H_e, respectively, were observed, showing that the alkyl chain was in the deshielding region of the carbonyls. Those chemical shift changes suggest the bromophenyl pyridinium group was completely encapsulated in the cavity of CB[8] while the alkyl chain was outside the cavity, similar to CB[7]. As the NMR spectrum exhibited slow exchange, it was feasible to estimate the binding ratio of the BPTN⊂CB[8] complex to be 2:1 (Fig. S6, ESI†).

Subsequently, in order to further confirm the binding ratio of the host–guest complex, a Job's plot was performed using
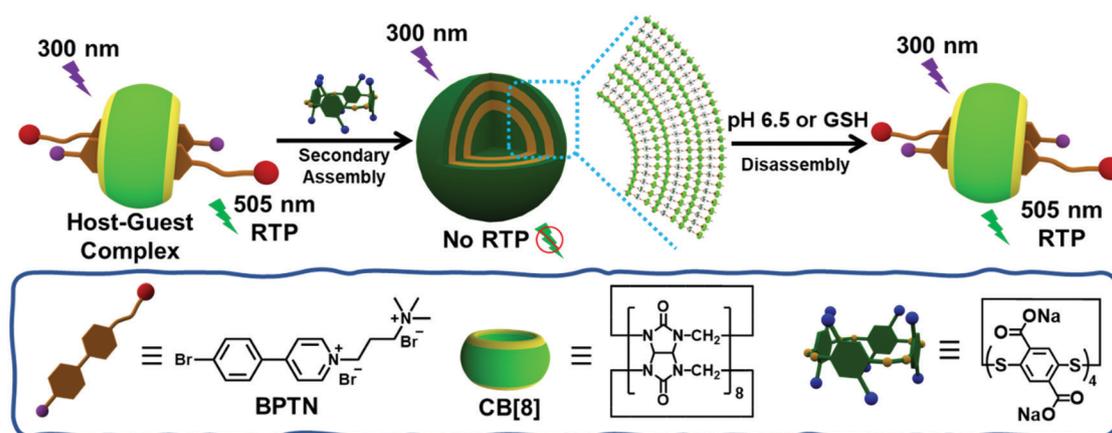

Scheme 1 Schematic illustration of biaxial pseudorotaxane supramolecular assembly and disassembly.

UV-Vis spectra. BPTN was determined to adopt a 1 : 1 stoichiometry ratio with CB[7] (Fig. S7, ESI†). Accompanied by the addition of CB[7], the band at 310 nm in the UV-Vis spectrum of bromophenyl pyridinium derivatives gradually decreased and exhibited a slight red shift (Fig. S8, ESI†). In contrast, consistent with the results of the NMR experiments, BPTN was determined to adopt a 2 : 1 stoichiometric ratio with CB[8] (Fig. 1b). That is to say, BPTN and CB[8] formed biaxial pseudorotaxane by host–guest interaction. With the gradual addition of CB[8], the adsorption bands of BPTN around 310 nm decreased with a slight red-shift (Fig. S9, ESI†). Next, the optical properties of BPTN and its complexes with CB[7] and CB[8] were examined by photoluminescence spectra, fluorescence spectra and time-lapse photoluminescence spectra. Simultaneously, the binding constant (K) was determined using the nonlinear least-squares fitting method according to the photoluminescence spectra. The binding constant of BPTN and CB[7] was $K = (2.02 \pm 0.52) \times 10^7$ M^{-1} (Fig. 1c), while the binding constants of BPTN and CB[8] were $K_1 = (1.09 \pm 0.42) \times 10^6$ M^{-1} and $K_2 = (3.00 \pm 0.20) \times 10^5$ M^{-1} (Fig. 1d). The photoluminescence spectra and excitation spectrum of BPTN upon addition of CB[8] are shown in Fig. 2a and Fig. S10 (ESI†). For free BPTN, the photoluminescence spectra only showed fluorescence at around 380 nm, which was consistent with its fluorescence spectrum (Fig. S11, ESI†). Exhilaratingly, the intensity of fluorescence gradually decreased, and a new emission peak appeared around 505 nm with the addition of CB[8]. Further time-lapse photoluminescence spectra (delayed by 0.2 ms) preliminarily confirmed that the emission peak around 505 nm was the phosphorescent emission of BPTN⊂CB[8] (Fig. 2b). The intensity of green emission increased markedly under an argon atmosphere, indicating that argon shielded the

oxygen and reduced the quenching of triplet electrons (Fig. 2c). With a decrease in temperature, the green emission was also significantly enhanced, which ruled out the possibility of thermally activated delayed fluorescence (Fig. S12, ESI†). Then, the time-resolved fluorescence decay curves were tested (Fig. 2d). Based on this, the lifetime at 505 nm of BPTN⊂CB[8] was found to be 602 μs. Moreover, the phosphorescence quantum yield was measured to be 2.10% (Fig. S13, ESI†). As for CB[7], with the addition of CB[7], the bands around 380 nm and 505 nm in the photoluminescence spectra of BPTN were slightly increased (Fig. S14, ESI†). By analyzing the fluorescence spectra and time-lapse photoluminescence spectra of BPTN⊂CB[7], the emission peaks at 380 nm and 505 nm could be attributed to fluorescence emission and phosphorescence emission, respectively (Fig. S15, ESI†). Combining the above experimental results, effective RTP in water could be achieved with a complex of CB[8] and BPTN, which was much stronger than the complex with CB[7].

In order to further study the co-assembly behavior between BPTN⊂CB[8] and SSP[4], we first studied the optical transparency of the co-assembly. With the addition of SSP[4] to a PBS solution of BPTN⊂CB[8], the transmittance decreased significantly (Fig. 3a). At the same time, the obtained solution of the ternary assembly showed an obvious Tyndall effect, which also proved the generation of aggregates (Fig. S16, ESI†). Furthermore, dynamic light scattering (DLS) experiments were carried out to study the size distribution of the assembly (Fig. 3b). Initially, the inclusion complex was only distributed in the small size region. However, after adding SSP[4], the ternary assembly had a larger size, showing that the average hydrodynamic diameter of BPTN⊂CB[8]@SSP[4] was about 430 nm.
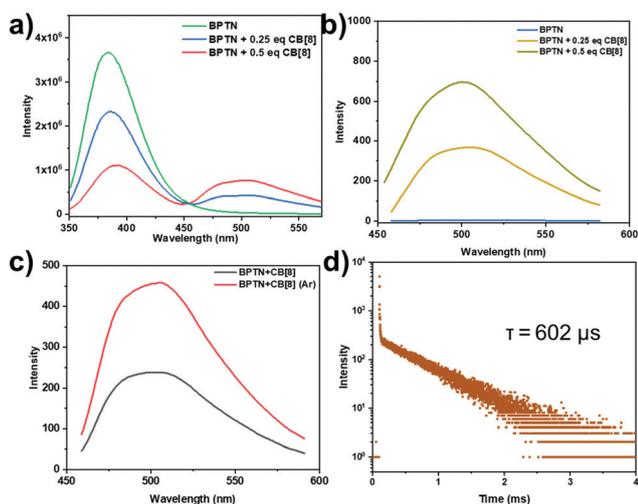
Fig. 2 (a) Photoluminescence spectra of BPTN (10 μM) and CB[8] at concentrations of 0, 2.5 and 5 μM in PBS solution; (b) time-lapse photoluminescence spectra of BPTN (10 μM) and CB[8] at concentrations of 0, 2.5 and 5 μM (delayed by 0.2 ms) in PBS solution; (c) time-lapse photoluminescence spectra of BPPY⊂CB[8] under atmosphere and argon in PBS solution; (d) time resolved photoluminescence decay curves of BPTN⊂CB[8] at 505 nm ([BPTN] = 2[CB[8]] = 10 μM) in PBS solution.
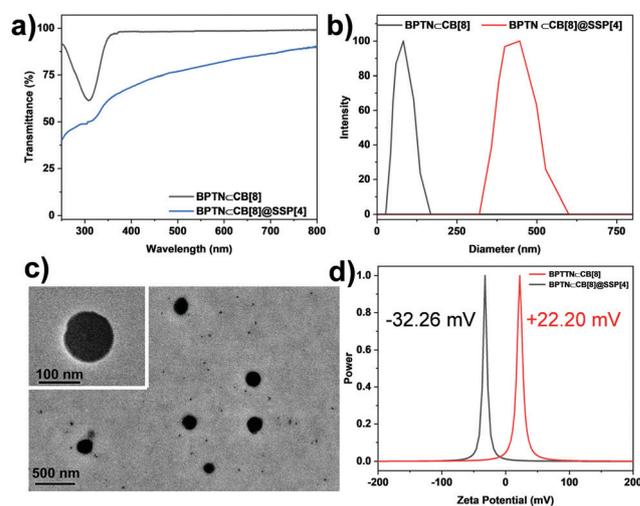
Fig. 3 (a) Optical transmittance of BPTN⊂CB[8] and BPTN⊂CB[8]@SSP[4] in PBS solution ([BPTN] = 2[CB[8]] = 10 μM, [SSP[4]] = 20 μM); (b) DLS data of BPTN⊂CB[8] and BPTN⊂CB[8]@SSP[4] in PBS solution ([BPTN] = 2[CB[8]] = 10 μM, [SSP[4]] = 20 μM); (c) TEM images of BPTN⊂CB[8]@SSP[4] (the inserted image is an image of the nanoparticles at a different scale); (d) zeta potential of BPTN⊂CB[8] and BPTN⊂CB[8]@SSP[4] in PBS solution ([BPTN] = 2[CB[8]] = 10 μM, [SSP[4]] = 20 μM).
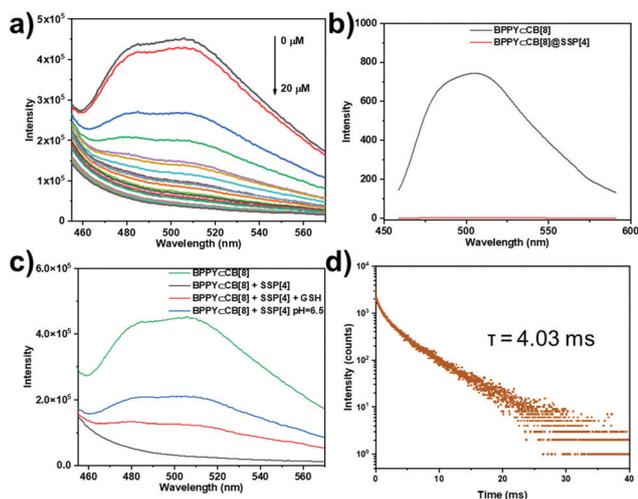
In addition, a transmission electron microscope (TEM) gave intuitive morphological information, displaying spherical nanoparticles (Fig. 3c) with diameters of about 250 nm. Thus, the supramolecular biaxial pseudorotaxane co-assembled with SSP[4] forming nanoparticles. With the addition of SSP[4], the zeta potential of the assembly changed from positive 22.20 mV at the beginning to negative 32.26 mV (Fig. 3d), which also indicated the formation of a ternary supramolecular assembly.

Next, we studied the effect of BPTN⊂CB[8] after co-assembly with SSP[4] on phosphorescent emission behavior. With the gradual addition of SSP[4], the phosphorescence of BPTN⊂CB[8] gradually decreases to disappearance (Fig. 4a). To quantify the sensitivity of the supramolecular assembly to SSP[4], $\frac{P_0}{P}$ was defined as the ratio of phosphorescence intensity at 505 nm (P_0) to that with different concentrations of SSP[4] (P). The dependence of $\frac{P_0}{P}$ as a function of the concentration of SSP[4] ([SSP[4]]) was quantitatively analyzed according to the Stern–Volmer equation

$$\frac{P_0}{P} = 1 + K_{sv}[SSP[4]]$$

where K_{sv} is the Stern–Volmer constant showing the quenching efficiency of SSP[4] towards BPTN⊂CB[8] (Fig. S17, ESI†). On the other hand, the sensitivity of the supramolecular assembly toward SSP[4] can be expressed by the overall quenching response to SSP[4]
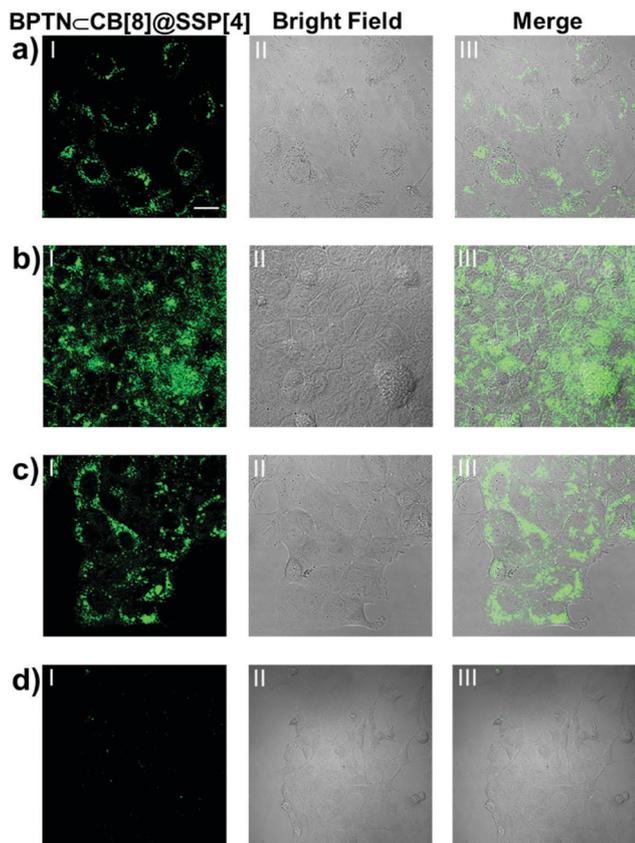
$$Q = \frac{P_0 - P_{SSP[4]}}{P_0} \times 100\%$$

where Q is the quenching efficiency, and P_0 and $P_{SSP[4]}$ are the phosphorescence intensities of BPTN⊂CB[8] and BPTN⊂CB[8]@SSP[4] in PBS solutions, respectively. In consequence, the quenching efficiency (Q) was calculated to be 92.4%, indicating that the supramolecular assembly was extremely sensitive to SSP[4]. When the concentration of SSP[4] was greater than 15 μM, the phosphorescence of the system was almost completely quenched. The time-lapse spectroscopy (delayed by 0.2 ms) also showed that the ternary supramolecular aggregates showed no phosphorescent emission (Fig. 4b).

Considering that the carboxyl unit and disulfide bond of SSP[4] are responsive to pH and a reduction in GSH, respectively, we speculated that a weakly acidic environment or the addition of GSH could restore the phosphorescence emission of the supramolecular system. Firstly, we studied the effect of a weakly acidic environment and GSH on the assembly behavior of the supramolecular aggregates. Regardless of adjusting the pH of the system to 6.5 or adding GSH, disassembly of supramolecular aggregates occurred, manifested in the size distribution around 200 nm, as shown by the DLS experiment (Fig. S18, ESI†). In addition, the Tyndall phenomenon of the solution had significantly weakened (Fig. S19, ESI†). Then, as expected, after adjusting the pH to 6.5 or adding GSH, both systems regained an emission peak around 505 nm (Fig. 4c). In order to confirm that this emission peak was phosphorescent emission, time-lapse spectra under a nitrogen atmosphere were obtained (Fig. S20, ESI†). In an argon atmosphere, the intensity of the emission peak around 505 nm increased significantly, which means that the phosphorescent emission was restored in the supramolecular stimuli-responsive system. Moreover, the phosphorescence lifetime of this assembly was determined to be $\tau = 4.03$ ms from the time-resolved photoluminescence decay curve, much longer than for the complex of BPTN⊂CB[8] (Fig. 4d), which was an order of magnitude transition from microseconds to milliseconds. The increase in phosphorescent lifetime may be attributed to the assembly formed by the BPTN⊂CB[8] complex and fragmented SSP[4] through electrostatic interaction. Compared with the initial phosphorescence of BPTN⊂CB[8], the recovery of phosphorescence quantum yield was reduced, but the lifetime expectancy was increased (Fig. S21, S22 and Table S1, ESI†). In summary, the supramolecular ternary assembly we constructed can emit effective phosphorescence with a long lifetime in response to a weakly acidic environment and GSH.

Encouraged by the above experimental results, we envisioned applying this supramolecular multilayer assembly to the phosphorescence imaging of living cells. A tumor microenvironment usually has acidic intercellular pH, high cytosolic GSH concentration and so on.[31–34] Therefore, such endogenous stimuli provide a prerequisite for our supramolecular nanoparticles to be used for phosphorescent imaging in targeted cancer cells. Human lung cancer (A549) cells, human cervical cancer (HeLa) cells, human breast cancer (MCF-7) cells and human kidney (293T) cells were selected for laser confocal imaging and cytotoxicity experiments using a standard CCK-8 assay. Although the guest BPTN displayed slight cytotoxicity,

Fig. 4 (a) Photoluminescence spectra of BPTN⊂CB[8] (10 μM) and SSP[4] at concentrations in the range from 0 to 20 μM in PBS solution; (b) Time-lapse photoluminescence spectra of BPTN⊂CB[8] and BPTN⊂CB[8]@SSP[4] in PBS solution ([BPTN] = 2[CB[8]] = 10 μM, [SSP[4]] = 20 μM); (c) Photoluminescence spectra of BPTN⊂CB[8], BPTN⊂CB[8]@SSP[4], BPTN⊂CB[8]@SSP[4] with GSH in PBS solution and BPTN⊂CB[8]@SSP[4] in PBS solution (pH = 6.5) ([BPTN] = 2[CB[8]] = 10 μM, [SSP[4]] = 20 μM, [GSH] = 2 mM); (d) time-resolved photoluminescence decay curves of BPTN⊂CB[8]@SSP[4] with GSH in PBS solution ([BPTN] = 2[CB[8]] = 10 μM, [SSP[4]] = 20 μM, [GSH] = 2 mM).

Fig. 5 Confocal fluorescence images of living (a) A549, (b) HeLa, (c) MCF-7 and (d) 293T cells incubated with BPTN⊂CB[8]@SSP[4] (scale bar = 20 μm). Figures (I) are green channel (λ_{ex} = 405 nm, λ_{em} = 450–550 nm) corresponding to the phosphorescent emission of the supramolecular assembly; figures (II) are the images of cells in the bright field; figures (III) are overlay images of green channels and bright field.

this assembly showed good biocompatibility, with no obvious toxicity to cells in the concentration range of this work (Fig. S23, ESI†). Even if the concentration of the assembly was increased to 50 μM, this system showed only negligible cytotoxicity with about a 90% cell survival rate. After which, all cancer cells were incubated with BPTN⊂CB[8]@SSP[4] for 24 hours, showing bright green phosphorescence in the cytoplasm by laser confocal microscopy (Fig. 5a–c). As a comparison, A549 cells treated with BPTN or BPTN@SSP[4] did not exhibit obvious green phosphorescence (Fig. S24, ESI†). Remarkably, there was no observable green phosphorescence in 293T cells treated with BPTN⊂CB[8]@SSP[4] (Fig. 5d), showing that the process of phosphorescence recovery can only be achieved in cancer cells. Those cell experiments manifested that this supramolecular probe provides a unique and efficient pathway for efficient targeted phosphorescent imaging in living cancer cells.

Conclusion

In summary, we have constructed a supramolecular stimuli-response probe *via* host–guest and multivalent electrostatic interaction for targeted imaging in cancer cells. Under complexation with CB[8], a double cationic bromophenol pyridinium salt derivative showed strong green phosphorescence at 505 nm in aqueous solution. Then, the host–guest complex was further co-assembled with SSP[4] forming nanoparticles, accompanied by the quenching of the green phosphorescence. Remarkably, once exposed to the environment of a weak acid or a large amount of GSH, the phosphorescence of the supramolecular assembly was restored. As expected, such a supramolecular assembly can respond to the microenvironment of cancer cells rather than normal cells, achieving targeted imaging of cancer cells. Therefore, we believe that this work is valuable and will contribute to the field of targeted phosphorescence imaging and the construction of smart biomaterials.

Experimental

Materials and instruments

All chemicals were commercially available reagent grade and used without further purification, unless otherwise noted. SSP[4] was prepared according to the procedure reported in the literature.[29,30] PBS solution (pH 7.2, 0.01 M) was purchased from Solarbio Science & Technology Co., Ltd (Beijing). The PBS solution (pH 6.5) was regulated with hydrochloric acid. NMR spectra were recorded on a Bruker 400 MHz instrument. High resolution mass (HRMS) spectra were performed on a Varian 7.0T FTMS with an ESI source. TEM images were acquired by a high-resolution transmission electron microscope (Philips Tecnai G2 20S-TWIN microscope) operating at an accelerating voltage of 200 keV. The samples were prepared by placing a drop of solution onto a carbon-coated copper grid and air-dried. UV-Vis absorption and transmission spectra were recorded on a Shimadzu UV-3600 spectrophotometer in a quartz cell (light path 10 mm) at 298 K with a PTC-348WI temperature controller. Dynamic light scattering (DLS) was recorded on BI-200SM (Brookhaven Company) at 298 K. Photoluminescence spectra were measured on an FLS980 instrument (Edinburgh Instruments, Livingstone, UK). Fluorescence spectra and time-lapse photoluminescence spectra (delayed by 0.2 ms) were recorded in a conventional quartz cell (light path, 10 mm) at 298 K. Absolute phosphorescence and fluorescence quantum yields and lifetimes by means of time-correlated single photon counting were measured on an FS5 instrument (Edinburgh Instruments, Livingstone, UK). The zeta potentials were determined on a NanoBrook 173Plus at 298 K. Confocal florescence imaging was recorded with an Olympus FV1000.

Synthesis of BPTN

4-(4-Bromophenyl)-1-(3-bromopropyl)pyridinium[35] (100 mg, 1 mmol) was dissolved in dry DMF (30 mL), and trimethylamine (1 mL, 2 mol L^{-1}) in THF was added dropwise to the reaction solution at 273 K under argon. Then the solution was stirred overnight at room temperature. The obtained suspension was filtered, and the precipitate was washed with dried CH_3CN and ethyl ether yielding BPTN as a white solid (70 mg, 63%).

^{1}H NMR: (400 MHz, D_2O) δ = 8.86 (d, J = 7.2 Hz, 2H), 8.33 (d, J = 7.2 Hz, 2H), 7.79–7.84 (m, 4H), 4.69 (t, J = 8.0 Hz, 2H), 3.50–3.54 (m, 2H), 3.16 (s, 9H), 2.58–2.64 (m, 2H) ppm. ^{13}C NMR (100 MHz, D_2O) δ = 156.31, 144.25, 132.82, 132.68, 129.62, 126.80, 125.28, 62.49, 57.15, 53.10, 24.43 ppm. HR-MS (m/z): (ESI, H_2O) calculated for $[M-2Br^-]^{2+}$: 167.0517, found 167.0520.

Cell viability assay

To investigate the toxicity of BPTN⊂CB[8]@SSP[4], BPTN⊂CB[8] and BPTN to A549, HeLa, MCF-7 and 293T cells, the cells were cultured in 96-well plates in corresponding media containing 10% FBS and 1% pen strep for 24 h, and then the corresponding compounds with different concentrations were added into the wells. The cells were further cultured for 24 h, and then cell viability was examined using a CCK-8 assay kit (NCM Biotech, China).

Confocal laser imaging

The cells were precultured in confocal dishes with glass bottoms of size 20 mm for 24 h and then incubated with BPTN⊂CB[8]@SSP[4] ([BPTN] = 2[CB[8]] = 10 μM, [SSP[4]] = 20 μM) for another 24 h. The cells were washed three times with PBS solution and observed using the confocal laser scanning microscope.

Conflicts of interest

The authors declare no competing interests.

Acknowledgements

Notes and references

1 Y.-M. Zhang, Y.-H. Liu and Y. Liu, *Adv. Mater.*, 2020, **32**, e1806158.
2 Y.-H. Liu and Y. Liu, *J. Mater. Chem. B*, 2022, **10**, 958–965.
3 A. B. Cook and P. Decuzzi, *ACS Nano*, 2021, **15**, 2068–2098.
4 Y. Lu, A. A. Aimetti, R. Langer and Z. Gu, *Nat. Rev. Mater.*, 2016, **2**, 16075.
5 C. Luo, J. Sun, D. Liu, B. Sun, L. Miao, S. Musetti, J. Li, X. Han, Y. Du, L. Li, L. Huang and Z. He, *Nano Lett.*, 2016, **16**, 5401–5408.
6 Y. Wang, M. S. Shim, N. S. Levinson, H. W. Sung and Y. Xia, *Adv. Funct. Mater.*, 2014, **24**, 4206–4220.
7 T. Ji, Y. Zhao, Y. Ding and G. Nie, *Adv. Mater.*, 2013, **25**, 3508–3525.
8 Z. Li, N. Song and Y.-W. Yang, *Matter*, 2019, **1**, 345–368.
9 H. Zhang, F. Liang and Y. W. Yang, *Chem. – Eur. J.*, 2020, **26**, 198–205.
10 M. Tang, Y.-H. Liu, X.-M. Xu, Y.-M. Zhang and Y. Liu, *Bioorg. Med. Chem.*, 2022, **57**, 116649.
11 X. Zhen, R. Qu, W. Chen, W. Wu and X. Jiang, *Biomater. Sci.*, 2021, **9**, 285–300.
12 H. Jin, X. Jiang, Z. Sun and R. Gui, *Coord. Chem. Rev.*, 2021, **431**, 213694.
13 J. Yang, M. Fang and Z. Li, *Acc. Mater. Res.*, 2021, **2**, 644–654.
14 J. Wang, X.-Y. Lou, Y. Wang, J. Tang and Y.-W. Yang, *Macromol. Rapid Commun.*, 2021, **42**, e2100021.
15 W. Zhao, Z. He and B.-Z. Tang, *Nat. Rev. Mater.*, 2020, **5**, 869–885.
16 S. Mukherjee and P. Thilagar, *Chem. Commun.*, 2015, **51**, 10988–11003.
17 X.-K. Ma and Y. Liu, *Acc. Chem. Res.*, 2021, **54**, 3403–3414.
18 W.-L. Zhou, Y. Chen, Q. Yu, H. Zhang, Z.-X. Liu, X.-Y. Dai, J.-J. Li and Y. Liu, *Nat. Commun.*, 2020, **11**, 4655.
19 S. Garain, B. C. Garain, M. Eswaramoorthy, S. K. Pati and S. J. George, *Angew. Chem., Int. Ed.*, 2021, **60**, 19720–19724.
20 D.-A. Xu, Q.-Y. Zhou, X. Dai, X.-K. Ma, Y.-M. Zhang, X. Xu and Y. Liu, *Chin. Chem. Lett.*, 2021, **33**, 851–854.
21 Y. Wang, H. Gao, J. Yang, M. Fang, D. Ding, B.-Z. Tang and Z. Li, *Adv. Mater.*, 2021, **33**, e2007811.
22 P. L. Suarez, M. Garcia-Cortes, M. T. Fernandez-Arguelles, J. R. Encinar, M. Valledor, F. J. Ferrero, J. C. Campo and J. M. Costa-Fernandez, *Anal. Chim. Acta*, 2019, **1046**, 16–31.
23 G. Qu, Y. Zhang and X. Ma, *Chin. Chem. Lett.*, 2019, **30**, 1809–1814.
24 J. Wang, Z. Huang, X. Ma and H. Tian, *Angew. Chem., Int. Ed.*, 2020, **59**, 9928–9933.
25 D. Li, F. Lu, J. Wang, W. Hu, X.-M. Cao, X. Ma and H. Tian, *J. Am. Chem. Soc.*, 2018, **140**, 1916–1923.
26 H.-J. Yu, Q. Zhou, X. Dai, F.-F. Shen, Y.-M. Zhang, X. Xu and Y. Liu, *J. Am. Chem. Soc.*, 2021, **143**, 13887–13894.
27 K.-Y. Zhang, Q. Yu, H. Wei, S. Liu, Q. Zhao and W. Huang, *Chem. Rev.*, 2018, **118**, 1770–1839.
28 X. Zhen, Y. Tao, Z. An, P. Chen, C. Xu, R. Chen, W. Huang and K. Pu, *Adv. Mater.*, 2017, **29**, 1606665.
29 P. T. Skowron, M. Dumartin, E. Jeamet, F. Perret, C. Gourlaouen, A. Baudouin, B. Fenet, J. V. Naubron, F. Fotiadu, L. Vial and J. Leclaire, *J. Org. Chem.*, 2016, **81**, 654–661.
30 L. Vial, R. F. Ludlow, J. Leclaire, R. Perez-Fernandez and S. Otto, *J. Am. Chem. Soc.*, 2006, **128**, 10253–10257.
31 F. Y.-F. Lee, A. Vessey, E. Rofstad, D. W. Siemann and R. M. Sutherland, *Cancer Res.*, 1989, **49**, 5244–5248.
32 P. Mi, *Theranostics*, 2020, **10**, 4557–4588.
33 J. W. Wojtkowiak, J. M. Rothberg, V. Kumar, K. J. Schramm, E. Haller, J. B. Proemsey, M. C. Lloyd, B. F. Sloane and R. J. Gillies, *Cancer Res.*, 2012, **72**, 3938–3947.
34 J. Sun, K. Du, J. Diao, X. Cai, F. Feng and S. Wang, *Angew. Chem., Int. Ed.*, 2020, **59**, 12122–12128.
35 X.-K. Ma, W. Zhang, Z. Liu, H. Zhang, B. Zhang and Y. Liu, *Adv. Mater.*, 2021, **33**, e2007476.